A 200 mm Wafer-Scale Al_2O_3 Photonics Waveguide Technology for UV and Visible Applications

P. Neutens, E. Mafakheri, X. Zheng, P. Helin, Z. Jafari, C. Lin, G. Jeevanandam, Nga P. Pham, S. Fan, C. Su, R. Jansen, P. Van Dorpe, N. Le Thomas, and C. Haffner

***Abstract*—Low-loss, UV wavelength compatible Al_2O_3 photonic waveguides have been fabricated in a 200 mm CMOS pilot line. The Al_2O_3 waveguide layer optical properties and roughness were characterized by ellipsometry and AFM, respectively. Optical losses of the slab mode in the waveguide layer were studied by prism coupling. SiO_2-cladded Al_2O_3 waveguides were patterned on 200 mm wafers and propagation losses were measured at 266, 360, 450, 532 and 638 nm wavelengths. Wafer-level measurements for 360–638 nm show an average propagation loss below 0.6 dB/cm, while die-level measurements for 266 nm yield average propagation losses between 4.3 and 14.7 dB/cm. To study the dependence of the wave propagation on processing variations, large sets of Mach-Zehnder interferometers with varying arm lengths were measured at a wavelength of 360 nm, and the coherence length of the standard 450 nm wide and 110 nm high Al_2O_3 waveguide was calculated to be longer than 2.2 mm.**

***Index Terms*—Photonic waveguide, photonic materials, alumina, ultra-violet, low-loss, CMOS-compatible, fabrication, characterization.**

I. Introduction

INFORMATION processing, sensing and life science technologies are currently subject to a revolution driven by integrated photonics, which brings the unique properties of light to current electronic platforms. For instance, light is used to transmit information under negligible losses compared to electrical signals and enables the detection of molecules by their unique absorption fingerprint. However, each of the applications that benefit from optics operate at a specific wavelength. This requires the photonic circuit to comprise of waveguide materials that are tailormade for the target application. The material transparency is an adequacy for designing functional integrated photonics in a desired frequency range, the necessity is determined by the ability to incorporate the material within existing and well-established complementary metal-oxide semiconductor (CMOS) technology. An ideal photonics platform offers low-loss waveguides, light sources, switching elements, detectors, etc. Yet for silicon there are many challenges such as: high propagation losses ($>$ 1 dB/cm), low power handling and a limited transparency window (1.1 μm to 4 μm) [1], [2]. Due to these issues, silicon nitride (SiN) with its bandgap ranging from 4.6 eV to 5.3 eV [3], [4], [5], [6] has emerged as a promising new platform. And while it offers exceptionally low losses approaching 1 dB/m at telecommunication wavelengths, it suffers from high loss when approaching the blue side of the visible spectrum (i.e., $\sim$1 dB/cm at 532 nm [7] and $\sim$3 dB/cm at 0.45 μm [8]). However, there are emerging applications such as label free sensors or ionic chip-scale quantum computing components requiring UV and blue frequencies. For instance, doppler cooling and optical read out of ionic qubits based on 88Sr+ and 40Ca+ utilizes photons of wavelengths between 397-420 nm [9]. Thus, material platforms that offer UV waveguides will have a paramount role in bringing these applications into conventional photonic integrated circuits (PIC). The larger bandgap and lower refractive index of Al_2O_3 waveguides have enabled demonstrations of propagation losses as low as 2.8$\pm$0.3 dB/cm at 405 nm in single mode waveguides [10], [11]. On-Chip resonance-enhanced Raman spectroscopy is another application that can greatly benefit from working at UV wavelengths in the 200-300 nm range, as working at shorter wavelengths not only generates much stronger Raman signals, but also eliminates interference from background fluorescence [12]. In this publication, we demonstrate an alumina photonics technology, that enables single mode, low-loss operation for UV wavelengths, experimentally verified for wavelengths down to 266 nm.

II. Waveguide Design and Simulations

Most integrated photonic application require waveguides that operate in the single mode regime at the wavelength spectrum of interest. The Ansys Lumerical mode solver [13] was used to calculate the mode indices and field profiles. Single mode operation at the shortest wavelength of 266 nm require a layer thickness smaller than 130 nm. To have leeway for future tests at even shorter wavelengths, an alumina layer thickness of 110 nm is chosen. Fig. 1(a) and (b) show the mode index as a function of the waveguide width for this chosen thickness, for 266 and 360 nm wavelength, respectively. A single-mode cut-off

Received 13 April 2025; accepted 27 April 2025. Date of publication 9 May 2025; date of current version 21 May 2025. The work of E. Mafakheri was supported by the European Union HORIZON TMA MSCA Postdoctoral Fellowships - European Fellowships through the Marie Skłodowska-Curie Actions (MSCA) under Grant 101065967. *(P. Neutens and E. Mafakheri contributed equally to this work.) (Corresponding author: P. Neutens.)*

P. Neutens, E. Mafakheri, P. Helin, Z. Jafari, G. Jeevanandam, Nga P. Pham, R. Jansen, P. Van Dorpe, and C. Haffner are with imec, 3001 Leuven, Belgium (e-mail: pieter.neutens@imec.be).

X. Zheng, C. Lin, S. Fan, C. Su, and N. Le Thomas are with Ghent University, 9000 Ghent, Belgium.

This article has supplementary downloadable material available at https://doi.org/10.1109/JPHOT.2025.3568162, provided by the authors.

Digital Object Identifier 10.1109/JPHOT.2025.3568162

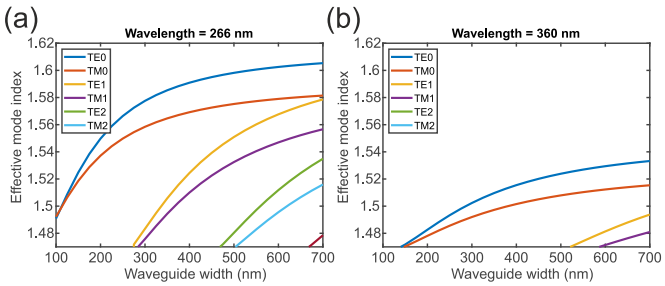

Fig. 1. Mode diagrams for 110 nm thick Al_2O_3 waveguides (a) for $\lambda = 266$ nm and (b) for $\lambda = 360$ nm.

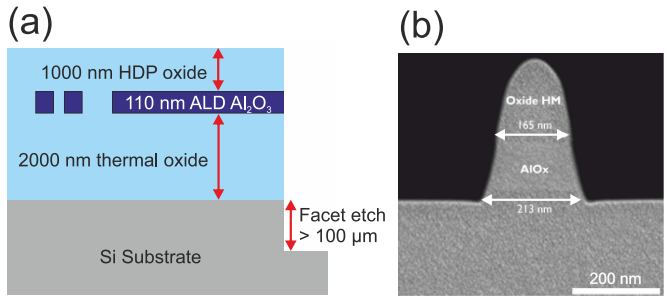

Fig. 2. (a) Schematic cross section of the Al_2O_3 integrated photonic waveguides. (b) Cross-section SEM of a 110 nm thick Al_2O_3 waveguide with a CD of 150 nm.

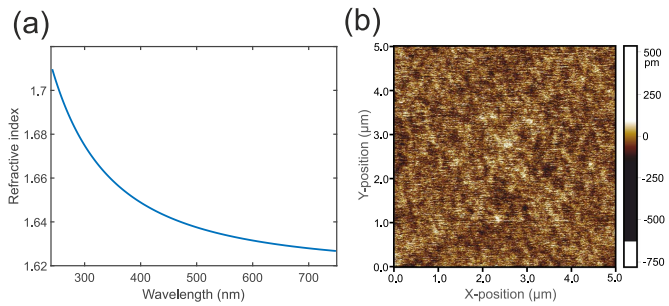

Fig. 3. (a) Optical properties of the Al_2O_3 waveguide layer measured by ellipsometry. (b) 1 μm $\times$ 1 μm AFM scan of the top surface of the Al_2O_3 waveguide layer, exhibiting an RMS roughness value of 0.29 nm.

waveguide width of 270 nm and 520 nm is found for 266 nm and 360 nm wavelength, respectively. To stay well below the multimode operation regime, a standard waveguide width of 450 nm was selected for the used integrated photonics components at $\lambda = 360$ nm (e.g., multimode interference (MMI) couplers and Mach Zehnder interferometers (MZI)). At the time of mask tape-out, no 266 nm laser was available. Therefore, the same waveguide widths are used for waveguide characterization at $\lambda = 266$ nm, being multimode at this wavelength. For propagation loss measurements at wavelengths of 450, 532 and 638 nm, single mode waveguide widths of 650, 1000 and 1400 nm were used.

Grating couplers were designed using Ansys Lumerical FDTD [13]. The full-etch grating couplers were designed for TE polarization and the corresponding period, linewidth and etch-depth was calculated for different wavelengths. Due to the limited index contrast between Al_2O_3 and the SiO_2 cladding, a moderate coupling efficiency of 10% was obtained in simulations for the main wavelength of 360 nm. The top and bottom cladding thicknesses were optimized to 1.06 μm and 2 μm to get maximum coupling efficiency, avoid any absorption by the silicon substrate and avoid metal-induced loss in case a metallic heater would be post-processed on the waveguides to include a thermal phase shifter. For edge coupling, an inverted taper design is used with a tip width of 130 nm, yielding a simulated 2.6 dB coupling loss for the 360 nm wavelength.

III. Waveguide Fabrication and Characterization

The integration process of the Al_2O_3 photonic waveguides was developed in the imec 200 mm CMOS pilot line. To implement photonic circuits in Al_2O_3, we started from a bare 200 mm silicon wafer, and grow a bottom cladding of 2000 nm thermal SiO_2. The waveguide layer of 110 nm Al_2O_3 was deposited by atomic layer deposition in a Beneq Transform tool. Patterning of the waveguides is realized by 193 nm lithography which allows to pattern structures as small as 130 nm, followed by reactive ion etching. Due to the low selectivity of the Al_2O_3 with respect to the photoresist during dry etching, we applied a SiO_2 hard mask. The SiO_2 hard mask was left after patterning the waveguide to be part of the top SiO_2 waveguide cladding. This ensured that no extra roughness or defects are created on the waveguide top surface during hard mask removal. High density plasma oxide deposition and planarization by chemical mechanical polishing was applied resulting in a cladding thickness of 1.06 μm. Finally, a facet etch was carried out in two steps, the first one was the oxide etch by deep RIE and followed by deep silicon etch to get mechanical clearance for the optical fiber for the edge couplers. The schematic cross-section of the fabricated photonic integrated circuit is shown in Fig. 2(a), and a cross-section scanning electron micrograph image of a 110 nm thick waveguide with critical dimensions of 150 nm can be seen in Fig. 2(b).

To characterize the waveguide layer, two techniques were used. The refractive index and thickness of the film were determined by ellipsometry and the film quality in terms of surface roughness was determined using atomic force microscopy (AFM). Slab mode propagation losses were determined by a Metricon 2010/M prism coupling setup for wavelengths of 406, 443 and 635 nm. Due to the lack of prisms for UV wavelengths, slab mode propagation loss measurements could not be extended to the UV range. Patterned waveguides for wavelengths of 360 nm and longer were measured by the cut-back method on an automated wafer-scale vertical fiber setup, while patterned waveguides for 266 nm wavelength were measured by free space edge coupling and imaging on die level.

IV. Experimental Results and Discussion

A. Characterization of the Al_2O_3 Thin Films

Ellipsometry measurements were performed on the as-deposited Al_2O_3 thin films. Fig. 3(a) shows the refractive index as a function of wavelength of the waveguide layer. A refractive

index of 1.693 and 1.656 were measured for wavelengths of 266 and 360 nm, respectively. A 49-point thickness measurement was performed on 110 nm Al_2O_3 directly deposited on a silicon wafer. An average thickness of 115 nm with standard deviation of 0.68 nm was obtained for a targeted thickness value of 110 nm. The film quality in terms of roughness for the ALD Al_2O_3 thin films was determined by AFM. To obtain a low scattering loss, both the bottom cladding SiO_2 and the Al_2O_3 waveguide layer should have an ultra-low roughness. The SiO_2 cladding roughness has been reported in a previous publication [14] and is known to have a low root mean square (RMS) roughness value of 0.13 nm for the 2 μm bottom cladding. The measured RMS roughness value of a 110 nm thick Al_2O_3 waveguide layer deposited as described in the fabrication section is shown in Fig. 3(b) for the centre location on the wafer. The measurements were done with the help of an AFM probe by scanning the top surface of the Al_2O_3 film over an area of 5 μm $\times$ 5 μm on 2 different positions of the 200 mm wafer (centre, and right). The RMS roughness values on the 2 positions are 0.089 and 0.090 nm.

B. Slab Mode Propagation Loss

As ellipsometry can't measure the extinction coefficient sufficiently accurate to predict the waveguide propagation loss, the slab mode propagation loss was characterized during the waveguide material development phase by means of a prism coupling setup. This allows for rapid waveguide material screening without requiring waveguide patterning. Due to the available prism materials and optics in the setup, measurements were possible with 406, 443 and 638 nm wavelengths. An Al_2O_3 film thickness of 250 nm was used, offering a good confinement for the TE0 mode allowing us to dominantly probe the intrinsic material loss. Fig. 4(a) and (b) display images of the propagating streak in the prism coupler setup for the 406 and 638 nm wavelength, respectively. Visually, a very slow decay of the scattered optical power as a function of the propagation distance is observed. In Fig. 4(c), the scattered optical power, collected by a moving fiber over 9 cm travel distance, has been plotted as a function of distance for 406, 443 and 638 nm, along with a fit with an exponential decay function, yielding propagation loss values of 0.58, 0.50 and 0.17 dB/cm, respectively.

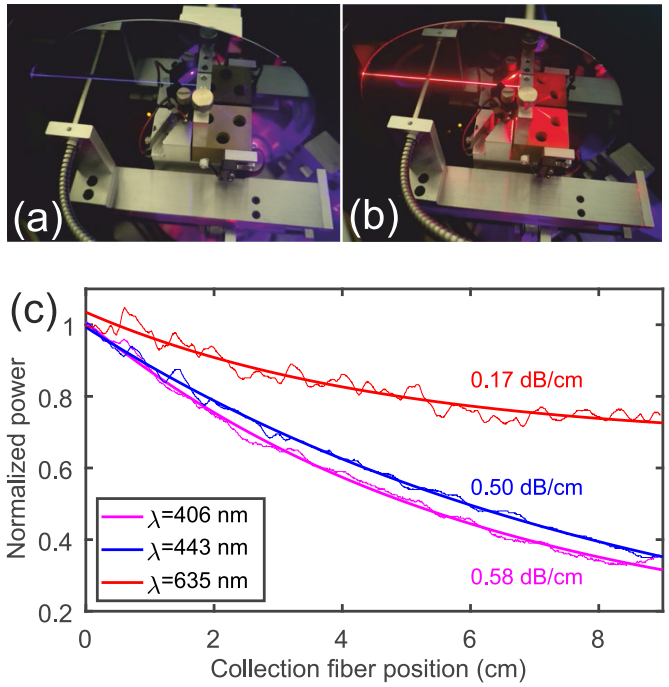

Fig. 4. Photographs of light propagation in the slab mode of a 250 nm thick Al_2O_3 waveguide layer on a 200 mm wafer for (a) 406 nm and (b) 635 nm wavelength. (c) Measurement of the scattered optical power as a function of the propagation distance for 406, 443 and 635 nm wavelengths, fitted by an exponential decay function.

C. Patterned Waveguide Propagation Loss

Having established low-loss slab mode propagation at blue wavelengths, a layout was designed to study the basic properties of Al_2O_3 rib waveguides for wavelengths of 266, 360, 450, 532 and 638 nm, with 360 nm as the main wavelength for this research. To measure the propagation loss for 360 nm, a set of 5 spiral waveguides is used with straight waveguide lengths of 0.05, 0.1, 1, 2 and 4 cm, and employ circular bends with a radius of 100 μm. This set is repeated for waveguide widths of 450, 500 and 600 nm. For 450 and 532 nm wavelength sets, the single mode waveguide widths are 650 and 1000 nm, respectively, and each set contains waveguides with lengths of 3.7, 4.5, 5.8 and 12.9 cm and a bend radius of 150 μm. Due to space limitations on the layout, only 2 spiral waveguide lengths of 5.7 and 8.5 cm with a bend radius of 250 μm were present for the 638 nm wavelength. For more information on the layout and measurement procedure, we refer to section S1 of the supplementary information. The transmitted optical power through all previously discussed spiral waveguides were measure for all dies on a 200 mm wafer, and propagation losses were determined by fitting a single exponential decay through the power as a function of waveguide length. Propagation loss wafer maps for 360 nm wavelength can be seen in Fig. 5(a), (b) and (c) for waveguide widths of 450, 500 and 600 nm, yielding loss values of 0.61 $\pm$ 0.31, 0.55 $\pm$ 0.18 and 0.44 $\pm$ 0.11 dB/cm, which are considerably lower than loss values reported in literature [10], [11], [14], [15], [16]. Fig. 5(d) and (e) display the propagation loss wafer maps for 450 and 532 nm, yielding values of 0.18 $\pm$ 0.10 and 0.03 $\pm$ 0.04 dB/cm for waveguide widths of 650 and 1000 nm respectively. Although propagation loss values for visible light are very low, one has to notice that because the layer thickness is optimized for UV wavelengths, this leads to low confinement factors ($n_{eff,450nm} = 1.482$, $n_{eff,532nm} = 1.480$) and small mode overlap with the etched waveguide sidewalls, leading to especially low propagation loss values at longer wavelengths. All propagation loss values are summarized in the boxplot displayed in Fig. 5(f). For the 638 nm wavelength, it was not possible to accurately determine the propagation loss, due to the ultra-low loss combined with the limited spiral waveguide length difference of 2.8 cm. From the analysis of the variation on the measured data and the variation measured on the grating coupling during the same run, we can only conclude that the

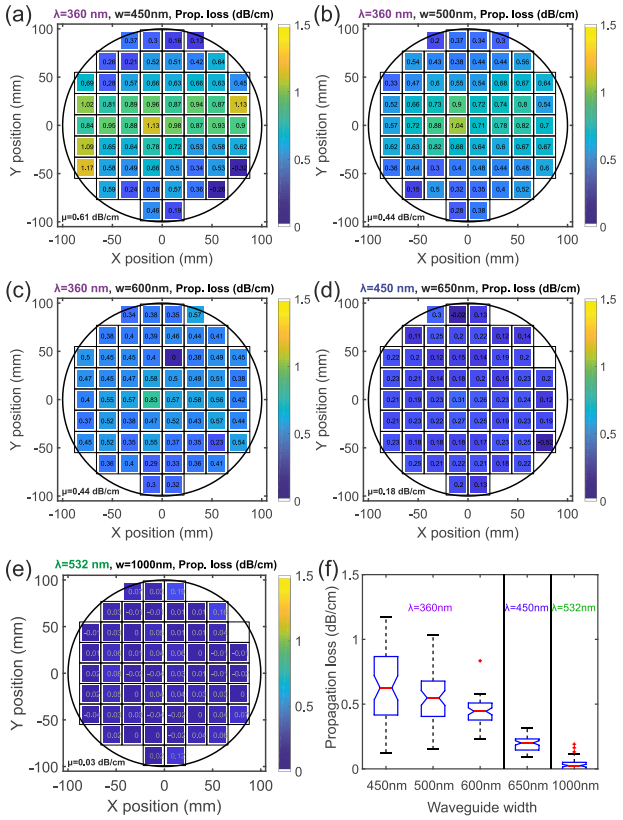

Fig. 5. Wafer-level propagation loss measurements for (a) $\lambda = 360$ nm, waveguide width $= 450$ nm, (b) $\lambda = 360$ nm, waveguide width $= 500$ nm, (c) $\lambda = 360$ nm, waveguide width $= 600$ nm, (d) $\lambda = 450$ nm, waveguide width $= 650$ nm, (e) $\lambda = 532$ nm, waveguide width $= 1000$ nm. (f) Overview of all measured propagation losses in a boxplot, indicating the median value and the 25th and 75th percentiles.

average propagation loss for 638 nm over all measured dies of the wafer is smaller than 0.16 dB/cm. Single-mode fiber-based measurements for 266 nm were not possible due to the lack of standard fibers available at short wavelengths and the very small grating coupler pitch being well below the lithography limit of the integration process. Hence, free space coupling combined with edge couplers was used to couple light in and from the chip. To investigate light propagation at 266 nm, we employ a Thorlabs 340UV-USB camera combined with the SMU-5X-UVB objective to analyze the scattered light from spiral waveguides with waveguide widths of 500 to 1100 nm. For this measurement, special care was taken to account for bend loss and avoid background light from non-ideal light coupling at the edge coupler. To mitigate these possible issues, a bend radius of 300 um was taken to minimize radiation losses and the edge coupler region was spatially offset from spiral region. More information about the layout and the measurement procedure can be found in section S1 of the supplementary information. A specific example of 266 nm wavelength light propagation in 500 nm × 110 nm and 1100 nm × 110 nm Al_2O_3 waveguides can be seen in Fig. 6(a). To extract the propagation loss, a superimage is created by combining several background-subtracted images taken with different integration times to get the highest signal-to-noise ratio for all sections of the waveguide. By fitting the

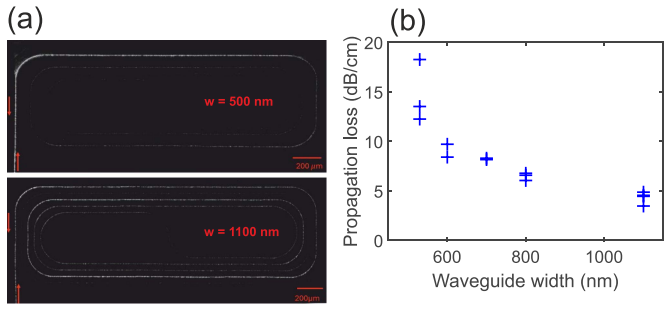

Fig. 6. (a) Image of light propagating in a 500 nm (top) and a 1100 nm (bottom) wide spiral waveguide at 266 nm wavelength. (b) Overview of the measured propagation losses at 266 nm.

resulting scattering power as a function of propagation distance with an exponential decay according to the Beer-Lambert law, we can extract the propagation loss. This measurement was repeated on a maximum of 4 dies for waveguide widths of 500, 600, 700, 800 and 1100 nm. In Fig. 6(b), propagation loss values are presented, yielding average values between 4.3 and 14.7 dB/cm, for waveguide widths of 1100 and 500 nm, respectively. This variation can be attributed to the increased mode overlap with the etched waveguide sidewalls, leading to higher scattering losses caused by sidewall roughness. This demonstrates that absorption losses in the presented 200 mm wafer-scale Al_2O_3 technology are lower than 4.3 dB/cm, allowing it to compete at UV-C wavelengths with silica based technologies offering propagation losses in the 3-4 dB/cm range [17].

D. Waveguide Coherence Length

Photonic integrated interferometers are widely used as filters, modulators and multiplexers in different application fields, going from life sciences to telecommunication. For this group of devices to exhibit a consistent and reliable operation, it is of paramount importance that the accumulated phase during propagation in the arms of the interferometer can be reproduced with very high precision. Variations in the waveguide's geometry and material composition cause fluctuations in its effective refractive index along the propagation direction, leading to the emergence of a random phase component $\Delta\phi$. This random phase component does not cancel out as light propagates through the waveguide; instead, it follows a random walk, with the mean-square phase deviation increasing with distance. In 1994, Adar et al. [18] have stated that this accumulation of random phase can be defined by a coherence length L_{coh}, defined as the length L for which $\langle \Delta\phi^2 \rangle$ of a batch of nominally identical waveguides equals 2 square rad. The coherence length is a fundamental parameter of a photonic waveguide, and characterizing it allows the design and fabrication of interferometer-based devices with a predictable and reproducible spectral performance.

In previous publications [18], [19], the coherence length is calculated based on the spectral response of a large batch of Mach-Zehnder interferometers. As we can only work with a single wavelength laser source at the used UV wavelength of 360 nm, we deduce the phase shift caused by processing variations from measuring the output powers of a large set of

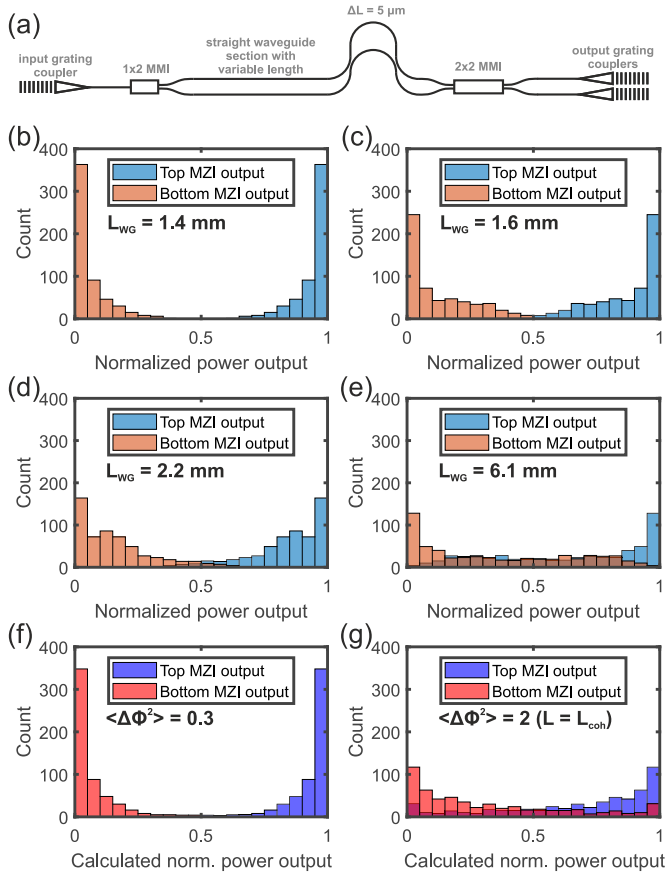

Fig. 7. (a) Schematic representation of the MZI used for the waveguide phase coherence study. (b-e) Histograms of the measured normalized powers for the top and bottom MZI outputs over a full 200 mm wafer. Each graph contains data for 560 MZI's (20 per die, 28 dies per wafer). The histogram is shown for MZI arm lengths of 1.4 (b), 1.6 (c), 2.2 (d) and 6.1 (e) mm. (f) Calculated distribution of the normalized output powers for a normal distribution of the phase difference with a variance of 0.3 (f) and 2.0 (g). The latter corresponds to the condition $L=L_{coh}$.

MZIs with varying arm lengths over a 200 mm wafer. On a single die, there are 4 sets of 20 MZI's with an arm length difference of 5 μm and a shortest arm length of 1.4, 1.6, 2.2 and 6.1 mm. As all 80 MZIs are measured on 28 dies with a fully automated photonics probe station, we obtain MZI output powers from 2240 devices, allowing us to make a statistically relevant calculation of the waveguide coherence length. The used laser is a CNI UV-FN-360 with a maximum output power of 50 mW and a spectral bandwidth of 7.2 pm, corresponding to a free space laser coherence length of 5.71 mm, effectively limiting the measurement for longer waveguide coherence lengths.

The schematic layout of the standard MZI is shown in Fig. 7(a). Splitting of the optical power equally over the two MZI arms is performed by a 1×2 MMI coupler and combining is done by a 2×2 MMI coupler. Both 1×2 and 2×2 MMI couplers were first characterized on wafers scale by means of a cascaded MMI tree, and mean insertion losses of 0.014 and 0.074 dB were measured for the nominal designs, respectively. The MZI contains four 90 degree circular bends with a radius of 100 μm, and the arm length difference of 5 μm is introduced in the vertical straight waveguide sections. For optimal 3-dB MMI couplers, the outputs of the interferometer with unity input can be expressed by

$$\left|E^2\right| = \frac{1}{2}\left(1 \pm \sin\left(\delta\phi\right)\right) \tag{1}$$

with $\delta\phi = \phi_1 - \phi_2$, the phase difference between both arms at the combiner input. Based on the measured MZI output powers and a reference power measurement from an adjacent reference waveguide of equal length, it is possible to calculate the phase difference $\delta\phi$, given that the phase difference in absence of phase variations lies in the linear regime of the sine function and the phase variation is sufficiently small to yield a single solution. The coherence length can be calculated from the linear regression of the variance $\langle\delta\phi(L)^2\rangle$ and L according to the following relationship [18].

$$\left\langle\delta\phi(L)^2\right\rangle = \frac{2L}{L_{coh}} \tag{2}$$

Fig. 7(b)–(e) show the distribution of the measured normalized power of the top and bottom outputs of all measured MZI's with arm lengths of 1.4 mm (b), 1.6 mm (c), 2.2 mm (d) and 6.1 mm (e). The blue bars represent $P_{top}/(P_{top}+P_{bottom})$ and the red bars $P_{bottom}/(P_{top}+P_{bottom})$. A clear increase in variation of the output power as a function of MZI arm length is observed. From measurements on the MZIs with shortest arm lengths (Fig. 7(b)), we also see that the arm length difference of 5 μm on average contributes to an initial situation close to constructive interference in the combiner towards the top MZI output. This initial condition prevents finding a unique solution of (1), and hence the phase difference cannot be calculated accurately. As both the measurement data of the shortest MZIs and the camera view confirm this initial state, we have calculated the expected output power distributions for this state with normally distributed phase differences for the same number of data points as obtained in the wafer scan. Fig. 7(f) displays the expected power distribution from the MZI outputs for $\langle\delta\phi(L)^2\rangle = 0.3$, corresponding well to the L = 1.4 mm measurement. Fig. 7(g) shows the expected power distribution for the condition $L = L_{coh}$ ($\langle\delta\phi(L)^2\rangle = 2$), corresponding well to the L = 6.1 mm measurement. Although the single wavelength measurements do not allow us to accurately derive the phase shift and perform the linear regression to determine the waveguide phase coherence length, from comparison of the measurements to the calculated power distributions, we can conclude that the measurement is most likely limited by the laser coherence length and that the phase coherence length for an Al_2O_3 waveguide with a 450 nm width and 110 nm height at a wavelength of 360 nm exceeds 2.2 mm.

V. Conclusion

We have demonstrated low-loss single-mode Al_2O_3 photonic wire waveguides fabricated in a CMOS pilot line for UV and visible wavelength applications. The Al_2O_3 thin film was measured to have a refractive index of 1.656 at 360 nm and it showed a very smooth surface (RMS roughness ~0.09 nm). The waveguide losses were measured using cutback method and were performed

at 266, 360, 450, 532 and 638 nm wavelengths for a 110 nm thick waveguide, showing sub-dB/cm operation for 360–638 nm wavelength and 4.3-14.7 dB/cm for 266 nm wavelength. A very large set of MZIs was measured to assess the coherence length of the standard 450 nm $\times$ 110 nm, revealing a coherence length exceeding 2.2 mm. Confirming reliable, low-loss operation for the 360–638 nm wavelength range, and propagation losses at 266 nm that are competitive with state-of-the-art silica waveguide shows that chip-based applications in sensing and quantum computing requiring UV or blue wavelengths are now achievable with a reliable, wafer-level Al_2O_3 photonic waveguide-based technology.

ACKNOWLEDGMENT

The author P. Neutens would like to thanks John O' Callaghan and Thijs Geurts for process integration support and material supply.

REFERENCES

[1] R. Kitamura, L. Pilon, and M. Jonasz, "Optical constants of silica glass from extreme ultraviolet to far infrared at near room temperature," *Appl. Opt.*, vol. 46, pp. 8118–8133, Nov. 2007.

[2] R. Soref, "Mid-infrared photonics in silicon and germanium," *Nat. Photon.*, vol. 4, pp. 495–497, Aug. 2010.

[3] L. Museur, A. Zerr, and A. Kanaev, "Photoluminescence and electronic transitions in cubic silicon nitride," *Sci. Reports*, vol. 6, 2016, Art. no. 18523.

[4] J. Bauer, "Optical properties band gap, and surface roughness of Si_3N_4," *Physica Status Solidi*, vol. 39, pp. 411–418, Feb. 1977.

[5] E. Vianello et al., "Explanation of the charge-trapping properties of silicon nitride storage layers for NVM devices part I: Experimental evidences from physical and electrical characterizations," *IEEE Trans. Electron Devices*, vol. 58, no. 8, pp. 2483–2489, Aug. 2011.

[6] A. Iqbal, W. B. Jackson, C. C. Tsai, J. W. Allen, and C. W. Bates Jr., "Electronic structure of silicon nitride and amorphous silicon/silicon nitride band offsets by electron spectroscopy," *J. Appl. Phys.*, vol. 61, pp. 2947–2954, Apr. 1987.

[7] A. Z. Subramanian et al., "Low-loss singlemode PECVD silicon nitride photonic wire waveguides for 532–900 nm wavelength window fabricated within a CMOS pilot line," *IEEE Photon. J.*, vol. 5, no. 6, Dec. 2013, Art. no. 2202809.

[8] P. Neutens et al., "Dual-wavelength neural probe for simultaneous opto-stimulation and recording fabricated in a monolithically integrated CMOS/photonics technology platform," in *Proc Int. Electron Devices Meeting*, 2023, pp. 1–4.

[9] K. K. Mehta, "Integrated optical quantum manipulation and measurement of trapped ions," Ph.D. dissertation, Dep. of Elect. Eng. and Comput. Sci. MIT, Cambridge, MA, USA, 2017.

[10] C. A. A. Franken et al., "Hybrid integrated near UV lasers using the deep-UV Al_2O_3 platform," 2023, *arXiv:2302.11492v1*.

[11] C. He et al., "Ultra-high Q alumina optical microresonators in the UV and blue bands," *Opt. Exp.*, vol. 31, no. 21, pp. 33923–33929, 2023.

[12] S. A. Asher, "UV resonance Raman spectroscopy for analytical, physical, and biophysical chemistry," *Anal. Chem.*, vol. 65, pp. 201A–210A, Feb. 1993.

[13] Lumerical Inc. [Online]. Available: https://optics.ansys.com/hc/en-us/articles/1500007184901-Lumerical-Citation-Instruction

[14] C. Sorace-Agaskar et al., "Versatile silicon nitride and alumina integrated photonic platforms for the ultraviolet to short-wave infrared," *IEEE J. Sel. Top. Quantum Electron.*, vol. 25, no. 5, Sep./Oct. 2019, Art. no. 8201515.

[15] G. N. West et al., "Low-loss integrated photonics for the blue and ultraviolet regime," *APL Photon.*, vol. 4, Jan. 2019, Art. no. 026101.

[16] M. M. Aslan et al., "Low-loss optical waveguides for the near ultra-violet and visible spectral regions with Al_2O_3 thin films from atomic layer deposition," *Thin Solid Films*, vol. 518, pp. 4935–4940, Jun. 2010.

[17] C. Su et al., "Low-loss and high-index contrast ultraviolet-C free-standing waveguides made of thermal silicon oxide," *Opt. Lett.*, vol. 49, pp. 3785–3788, Jun. 2024.

[18] R. Adar, C. H. Henry, M. A. Milbrodt, and R. C. Kistler, "Phase coherence of optical waveguides," *J. Lightw. Technol.*, vol. 12, no. 4, pp. 603–606, Apr. 1994.

[19] Y. Yang et al., "Phase coherence length in silicon photonic platform," *Opt. Exp.*, vol. 23, Jun. 2015, Art. no. 238353.